Supporting Information

2D Chiral Organic Salts with Large Piezoelectric Response

Hui-Peng Lv,‡ Zhi-Lin Liao,‡ Di Gao, Kai-Wen Jiang, Si-Qi Yu, Yi Lei, Jian-Chun Liu, Yi-Zhuo Geng, Yong Ai, Peng-Fei Li,* Yan Qin,* and Xiao-Gang Chen*

Ordered Matter Science Research Center, Nanchang University, Nanchang 330031, People's Republic of China.

E-mail: lipf@ncu.edu.cn, qinyan@ncu.edu.cn, chenxg@ncu.edu.cn

Experimental Section

Synthesis of *R*, *S*, and *Rac*-4-BrPEAC

All reagents were of analytical grade and used without further purification. *R*-, *S*-, or *Rac*-4-BrPEAC (50 mmol) was dissolved in ethanol. Hydrochloric acid (37% aqueous solution) was added dropwise, resulting in the formation of a white precipitate. Additional ethanol was then introduced until the precipitate completely dissolved, and the pH of the solution was adjusted to approximately 5~6. The mixture was filtered, and the filtrate was allowed to evaporate slowly at room temperature, yielding the corresponding high-quality single crystals of centimeter size.

Fabrication of *R*-4Br-PEAC/PDMS flexible film

Well-ground *R*-4-BrPEAC powders with weight ratios of 5, 10, 15, and 20 wt% were added to the PDMS precursor. Appropriate amounts of dichloromethane (DCM) were then introduced to form a homogeneous solution, which was stirred for 5 hours to ensure thorough mixing of the powders and PDMS. After DCM evaporation, 10 wt% hardener was added to the viscous liquid and stirred for precuring. The mixture was subsequently placed in a vacuum oven to remove residual DCM and air bubbles generated during stirring, before being spread onto a substrate to obtain a uniform film precursor with a thickness of 0.3 mm. Finally, the film precursor was transferred to a 100 °C oven for 1 hour for post-curing, yielding a uniform and elastic film. The composite films were cut into 2 cm × 2 cm pieces for further testing.

Methods

Single-crystal X-ray crystallography

Variable-temperature single-crystal X-ray diffraction data were gathered using a Rigaku XtaLAB Synergy-R/DW diffractometer. Data collection was conducted at a controlled temperature with a heating/cooling rate of 20 K/min. Data collection and structural refinement were performed using the Rigaku Crystal Clear and SHELXTL software package. The X-ray crystallographic structures have been deposited at the Cambridge Crystallographic Data Centre (deposition numbers CCDC: 2516741-2516747) and can be obtained free of charge from the CCDC via www.ccdc.cam.ac.uk/getstructures.

Powder X-ray diffraction

Variable-temperature powder X-ray diffraction (PXRD) data were collected by using a Rigaku D/MAX 2000 PC X-

ray diffraction system with Cu Kα radiation in the 2θ range of 5°-40° with a step size of 0.02°.

Second-Harmonic Generation (SHG)

Power-dependent and polarization-dependent SHG measurement was conducted on a home-built confocal scanning microscope. A 1064 nm picosecond laser (Rainbow 1064 OEM, NPI lasers) was used as an excitation source. A 50× objective (N.A. = 0.6, Nikon TU Plan ELWD) was selected to focus the laser onto the sample and collect the reflected SHG signals. The SHG signal was detected by a spectrograph (SpectraPro HRS-300, Teledyne Princeton Instruments). Polarization-dependent SHG measurement was realized by rotating a 1064 nm half-wave plate on the excitation path. Wavelength- dependent SHG measurement was performed by using a femtosecond laser (10W, < 290 fs, PHAROS, Light Conversion) equipped with an optical parametric amplifier (ORPHEUS, Light Conversion) system as the excitation source.

Resonance method

The impedance and phase angle spectra were characterized by an impedance analyzer (TH2851). The gold wires were attached to the ends of the crystal rod and clamped by the test fixture. The driving ac voltage was set as 1 V. The crystal rod size is 2.4 × 0.8 × 0.8 mm^3 and the length is along the *b*-axis. The calculation equations of the electromechanical coupling factor k_{33} and piezoelectric constant d_{33} are listed below.

$$k_{33}^2 = \frac{\pi f_r}{2 f_a} tan \frac{\pi \Delta f}{2 f_a}$$

$$s_{33}^D = \frac{1}{4\rho f_a^2 l^2}$$

$$s_{33}^E = s_{33}^D/(1 - k_{33}^2)$$

$$d_{33} = k_{33}\sqrt{\varepsilon_{33}^T s_{33}^E}$$

where ε_{33}^T is dielectric permittivity at free boundary condition, s_{33}^E and s_{33}^D are elastic compliance coefficients in short and open circuit conditions, respectively, Δf is the interval between f_r and f_a, ρ is the density, and l is the length of tested piezoelectric material. The ε_{33}^T value at 1 kHz (close to the free boundary condition) and room temperature was measured to be 9.84 via a LCR meter.

Scanning electron microscope (SEM) measurement

SEM characterization was performed using a Thermo Fisher Scientific Apreo 2C field-emission scanning electron microscope. High-resolution imaging was achieved with an accelerating voltage of 5 kV and a probe current of 0.8 nA. An Everhart-Thornley detector (ETD) was employed for secondary electron (SE) imaging to capture topographical contrast.

Piezoelectric output performance test

A sandwich structure was fabricated by stacking the *R*-4-BrPEAC/PDMS film between top and bottom copper tape electrodes. Two copper wires were attached to the electrode surfaces to connect to the test probe. The entire device was encapsulated with PET tape for testing. Periodic mechanical impacts were generated using a homemade electrodynamic shaker system with an adjustable force range of 2–8 N and a frequency of 10 Hz. Each test lasted 5 seconds. The output voltage was measured using an oscilloscope (Keysight DSOX3024T).

DFT calculations

The first-principles calculations were performed within the framework of density functional theory (DFT) implemented in the Vienna ab initio Simulation Package (VASP)[1-2] The exchange−correlation interactions were treated within the generalized gradient approximation of the Perdew−Burke−Ernzerhof type[3]. Van der Waals corrections are calculated based on DFT-D3 method with Becke-Jonson damping. The energy cut-off for the expansion of the wave functions was fixed to 550 eV. For the integrations over the k-space we used a 5x4x2 k-point mesh. The elastic stiffness is calculated with finite difference method.[4] The piezoelectric constants are calculated using density-functional perturbation theory.[5]

The elastic stiffness constants of point group 2 are presented as a 6 × 6 matrix:

$$\begin{bmatrix} c_{11} & c_{12} & c_{13} & 0 & c_{15} & 0 \\ c_{21} & c_{22} & c_{23} & 0 & c_{25} & 0 \\ c_{31} & c_{32} & c_{33} & 0 & c_{35} & 0 \\ 0 & 0 & 0 & c_{44} & 0 & c_{46} \\ c_{51} & c_{52} & c_{53} & 0 & c_{55} & 0 \\ 0 & 0 & 0 & c_{64} & 0 & c_{66} \end{bmatrix}$$

The piezoelectric strain constants of point group 2 can be described by a third rank tensor in the form of a 3 × 6 matrix:

$$\begin{bmatrix} 0 & 0 & 0 & d_{14} & 0 & d_{16} \\ d_{21} & d_{22} & d_{23} & 0 & d_{25} & 0 \\ 0 & 0 & 0 & d_{34} & 0 & d_{36} \end{bmatrix}$$

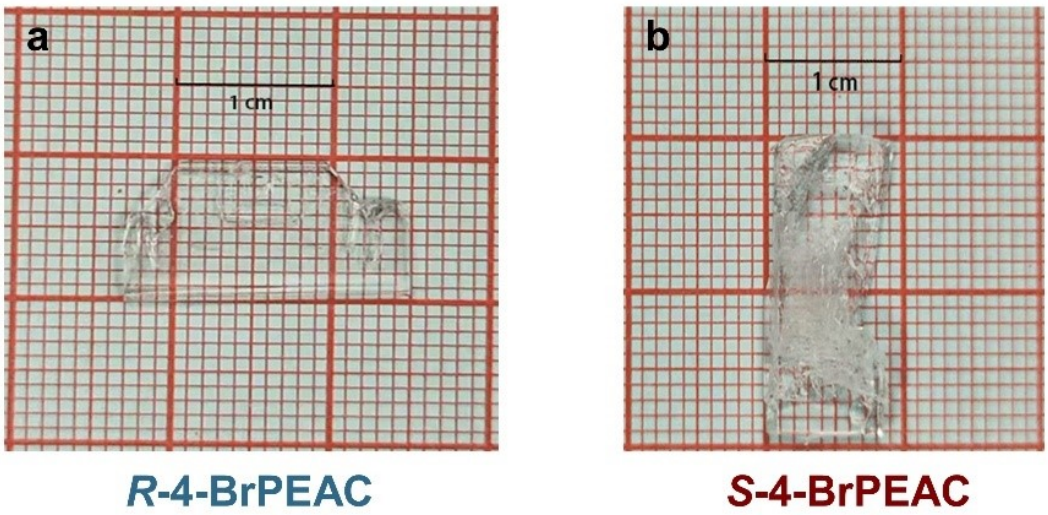

Fig. S1 Crystal images of *R* and *S*-4-BrPEAC.

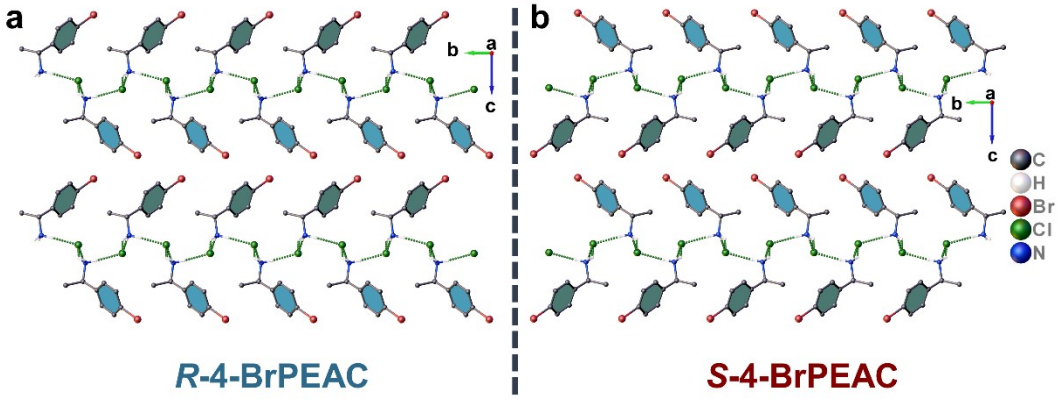

Fig. S2 A view of the crystal packing of (a) *R*- and (b) *S*-4-BrPEAC down the *bc* plane. Green dashed lines indicate N–H···Cl hydrogen-bonding interactions. Some hydrogen atoms are omitted for clarity. The grey dashed line indicates that the *R*- and *S*-4-BrPEAC structures are mirror images of each other.

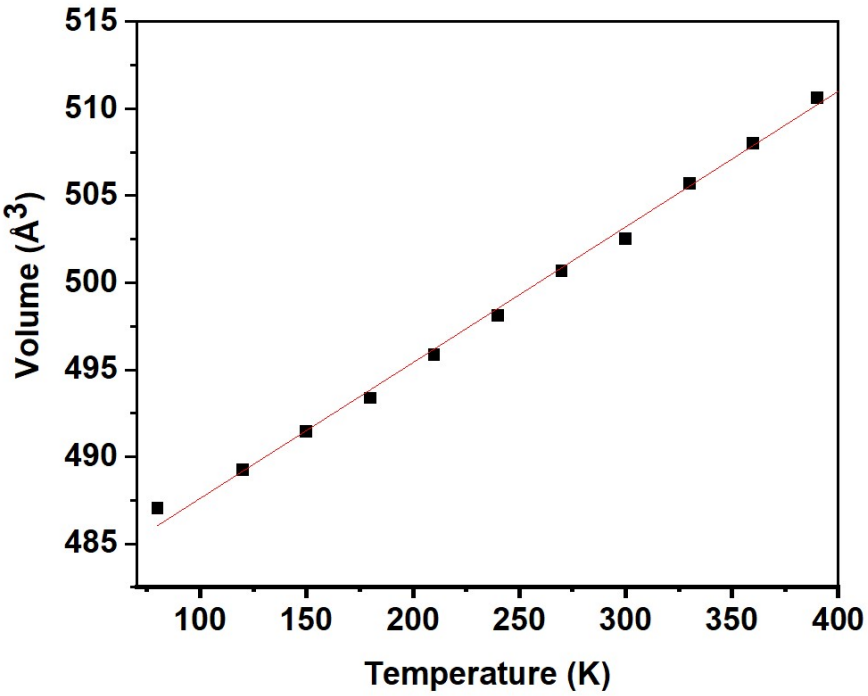

Fig. S3 Linear variation of volume as a function of temperature for *R*-4-BrPEAC.

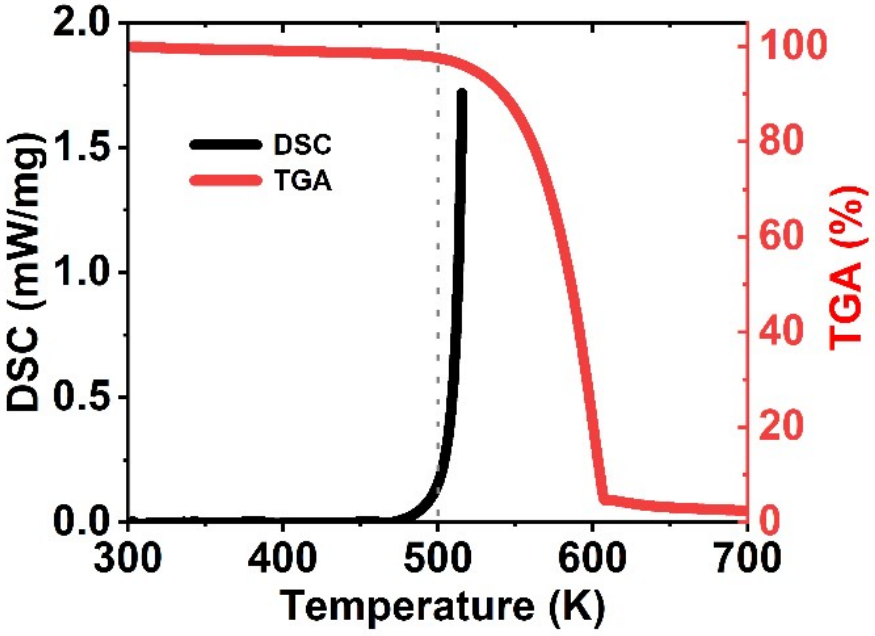

Fig. S4 DSC and TGA curves of *R*-4-BrPEAC.

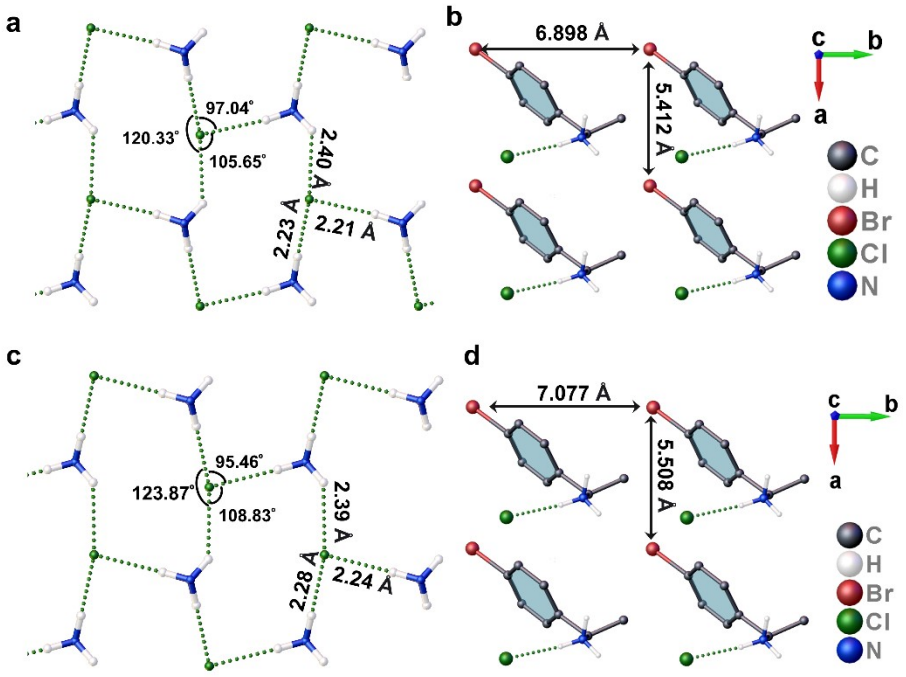

Fig. S5 Comparison diagram of the two-dimensional hydrogen-bonded network of *R*-4-BrPEAC at (a) 80 K and (c) 300 K and the spacing between Br atoms of adjacent cations at (b) 80 K and (d) 300 K.

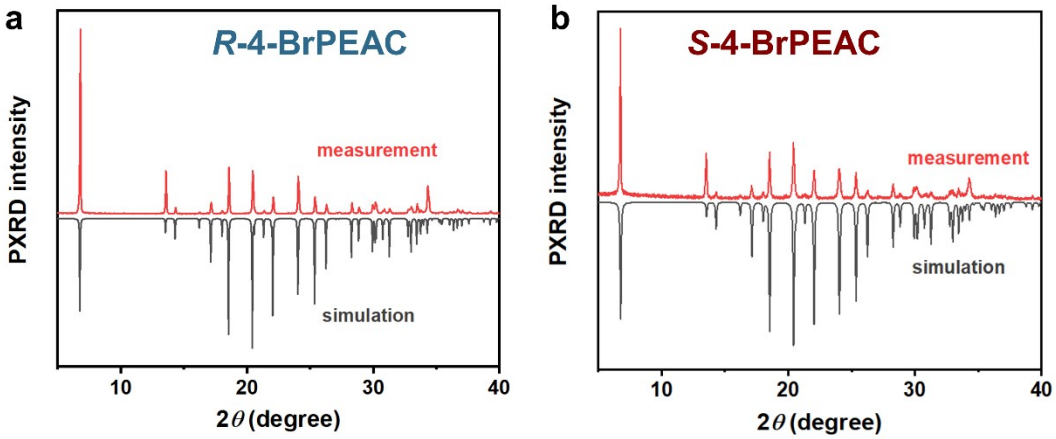

Fig. S6 The experimental PXRD pattern of (a) *R*- and (b) *S*-4-BrPEAC at 300 K matches well with its simulated PXRD pattern.

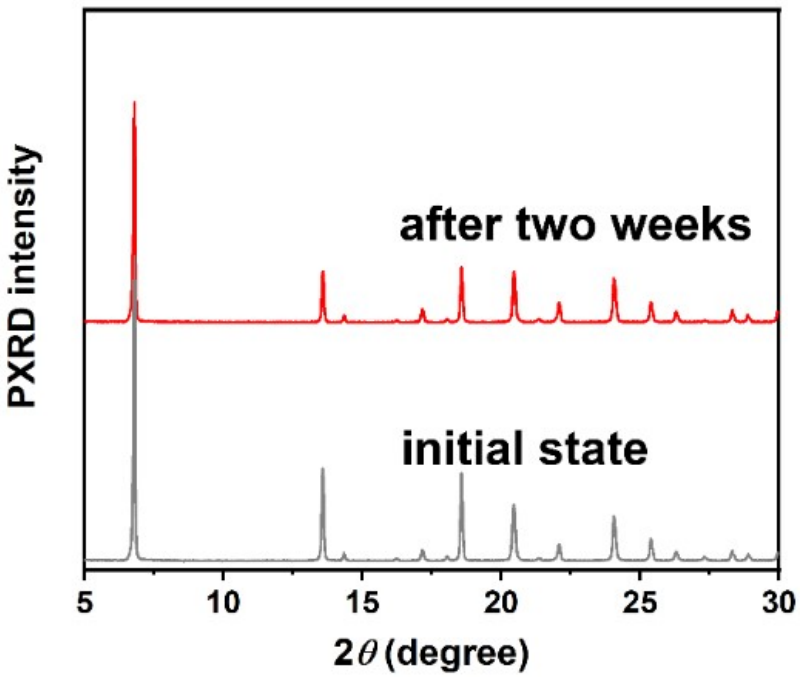

Fig. S7 PXRD patterns of the powder sample initially and after two weeks under ambient conditions. The patterns show no significant change, confirming the good stability of *R*-4-BrPEAC.

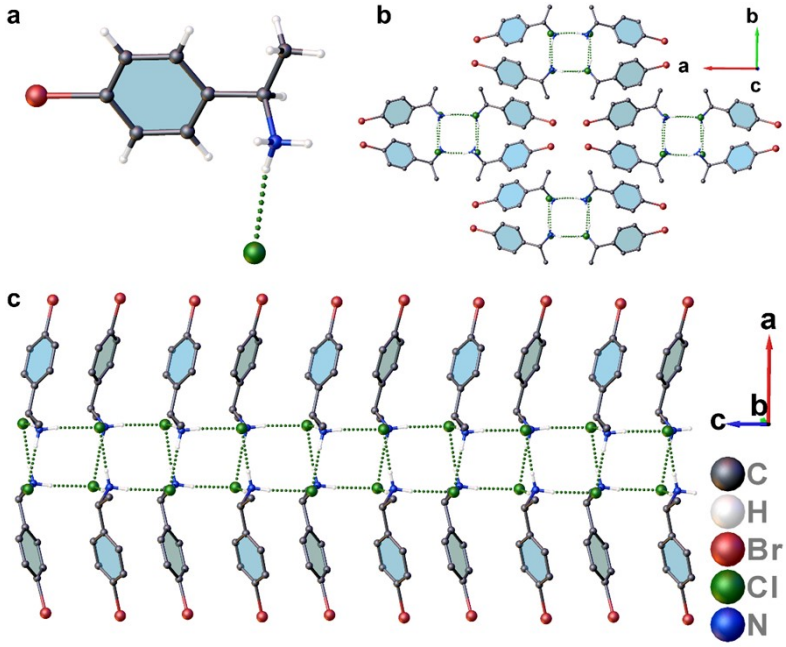

Fig. S8 Crystal structures of *Rac*-4-BrPEAC. (a) The asymmetric unit of *Rac*-4-BrPEAC. (b) A view of the crystal packing of *Rac*-4-BrPEAC down the *ab* plane. (c) A view of the crystal packing of *Rac*-4-BrPEAC down the *ac* plane, showing the 1D hydrogen-bonded chain. Green dashed lines indicate N–H···Cl hydrogen-bonding interactions. For clarity, some hydrogen atoms are omitted in (b) and (c).

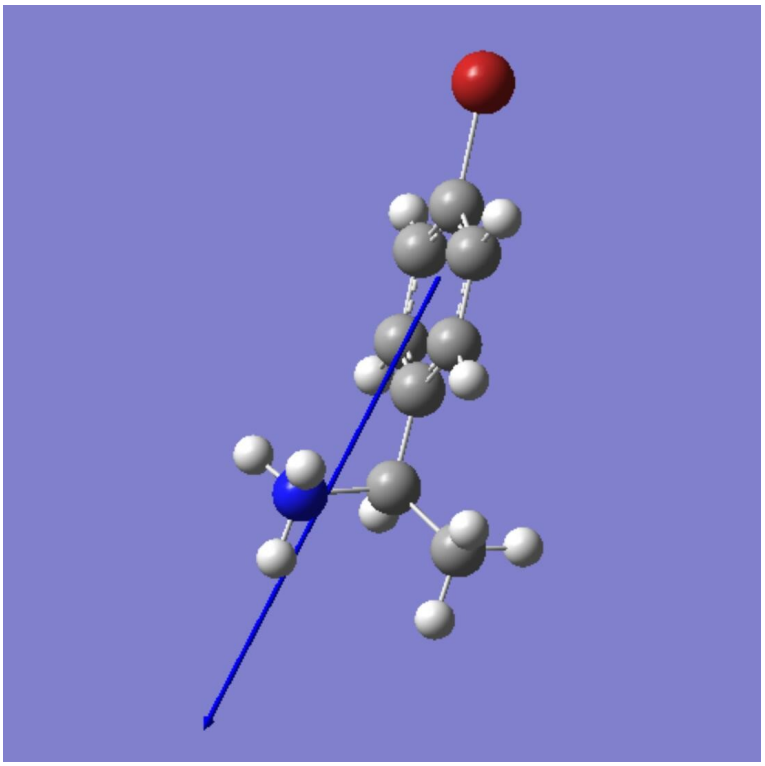

Fig. S9 The dipole vector of *R*-4-BrPEAC with a calculated dipole moment of 15.4 Debye.

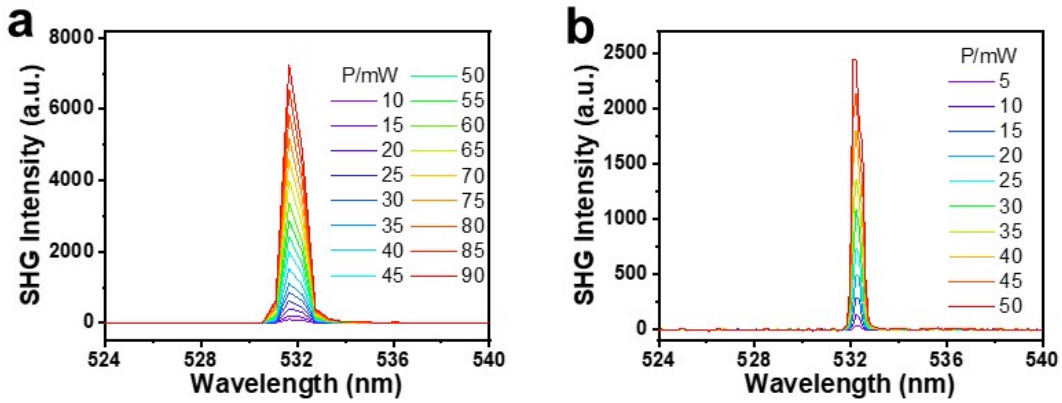

Fig. S10 SHG spectra of R (a) and S (b) crystals under various pump powers.

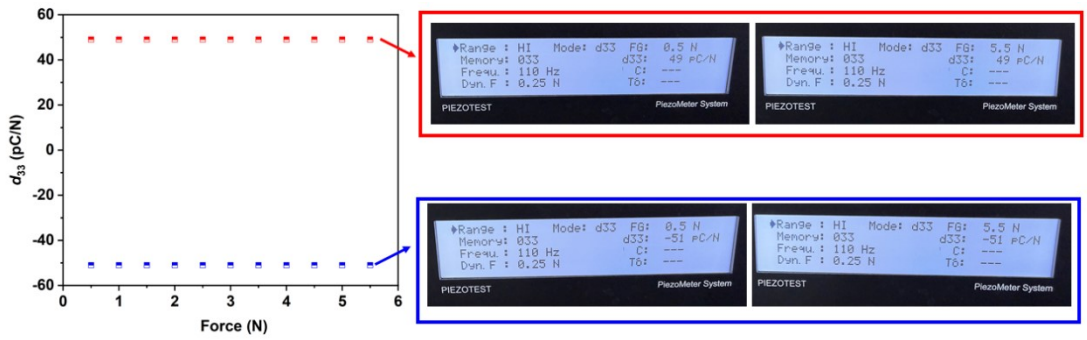

Fig. S11 The d_{33} values under different applied loading forces.

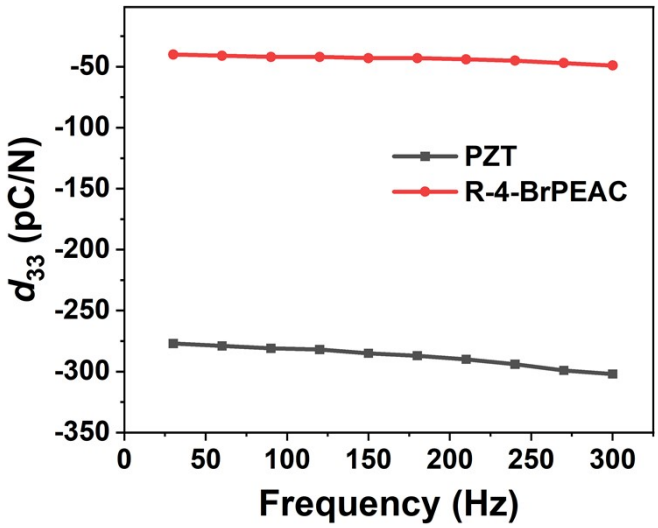

Fig. S12 Frequency dependence of piezoelectric constants of *R*-4-BrPEAC and PZT.

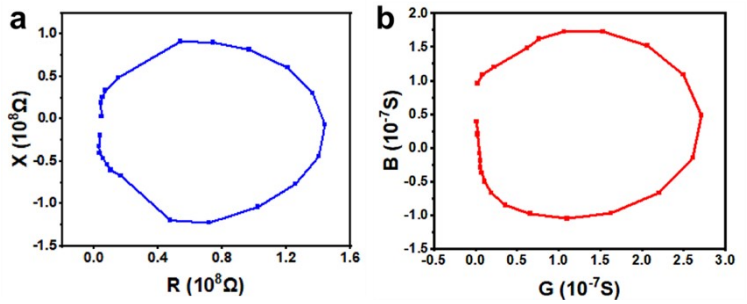

Fig. S13 Circular diagrams of impedance and admittance of *R*-4-BrPEAC crystal rod along *b*-axis.

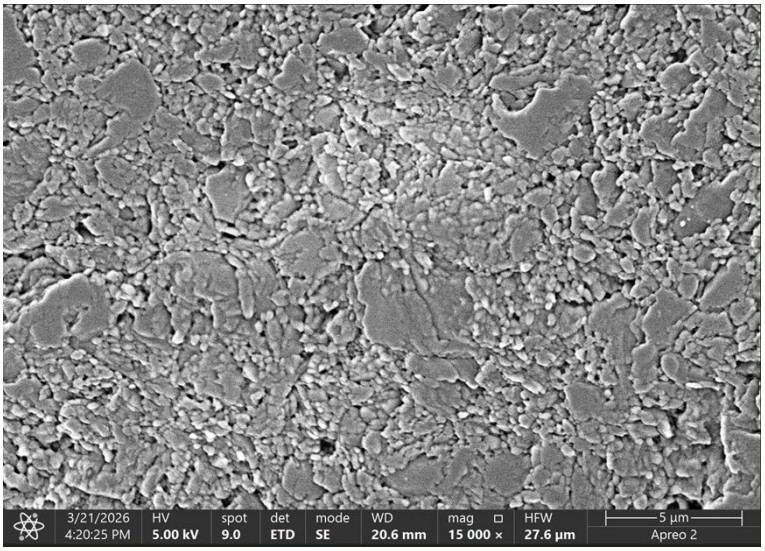

Fig. S14 SEM image of well-ground power pellet of *R*-4-BrPEAC for the fabrication of composite films.

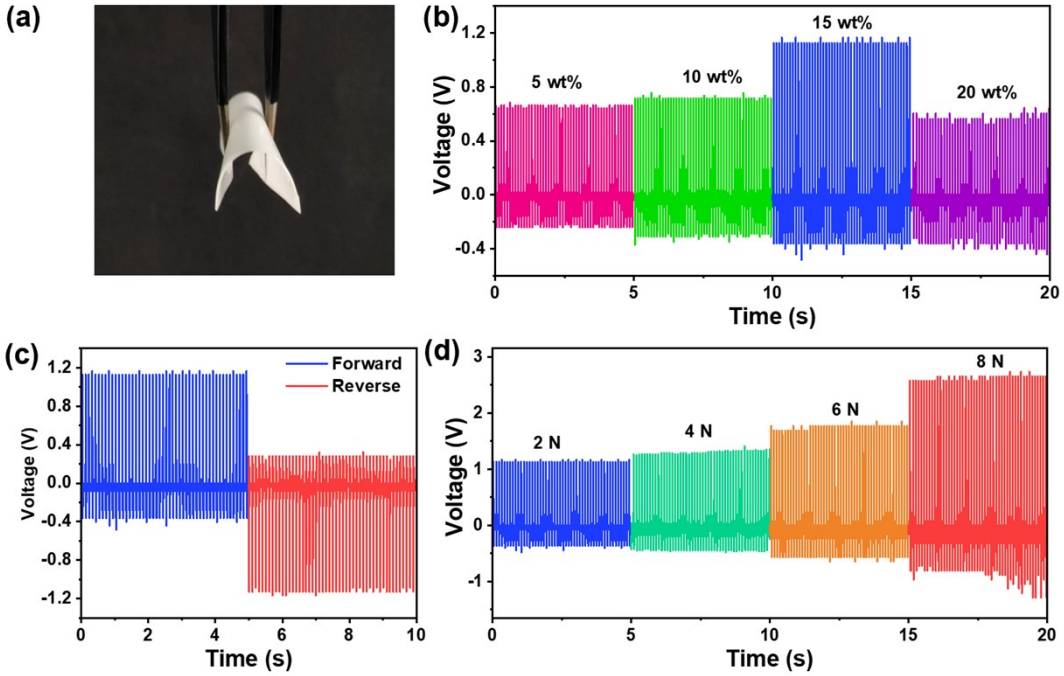

Fig. S15 (a) Photo of *R*-4-BrPEAC/PDMS composite film with weight ratio of 15 wt%. (b) Output voltage of *R*-4-BrPEAC/PDMS composite films with various weight ratio. (c) Output voltage of 15 wt% *R*-4-BrPEAC/PDMS composite film with both forward and reverse connections. (d) Output voltage of 15 wt% *R*-4-BrPEAC/PDMS composite film under different mechanical forces.

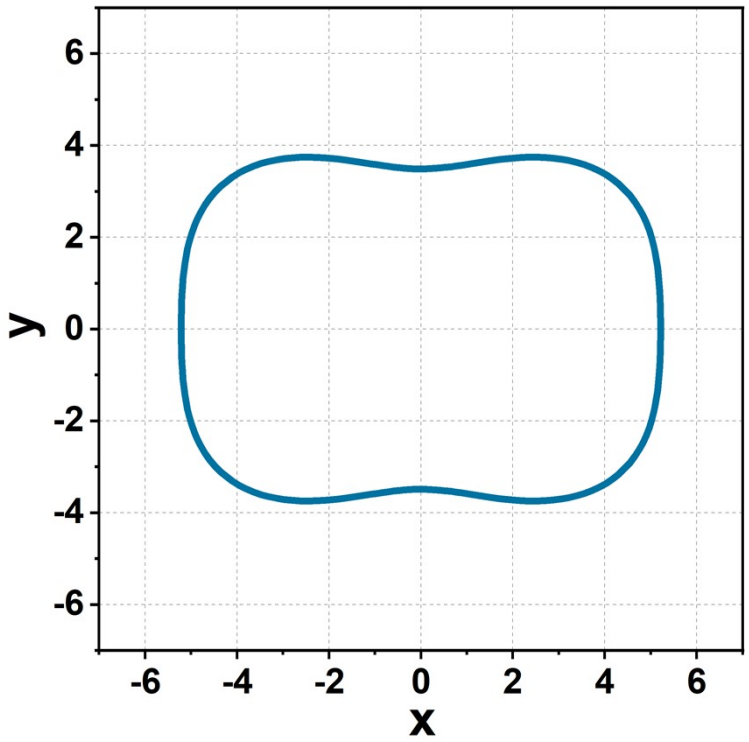

Fig. S16 Two-dimensional distribution of Young's modulus in the *xy*-plane.

Piezoelectric strain constant matrix $[d_{ij}]$:

$$\begin{bmatrix} 0 & 0 & 0 & -1.7 & 0 & 6.6 \\ -5.2 & -43.5 & 27.5 & 0 & 28.7 & 0 \\ 0 & 0 & 0 & 7.7 & 0 & -5.3 \end{bmatrix}$$

Elastic stiffness matrix $[c_{ij}]$:

$$\begin{bmatrix} 13.3 & 5.8 & 8.3 & 0 & 2.2 & 0 \\ 5.8 & 7.8 & 5.4 & 0 & 2.3 & 0 \\ 8.3 & 5.4 & 11.3 & 0 & -1.2 & 0 \\ 0 & 0 & 0 & 6.0 & 0 & 3.7 \\ 2.2 & 2.3 & -1.2 & 0 & 4.9 & 0 \\ 0 & 0 & 0 & 3.7 & 0 & 5.5 \end{bmatrix}$$

Table S1. Crystal data and structure refinement of *R*-4-BrPEAC at 80 K, 300 K and 390 K.

Temperature/K	80	300	390
Compound	*R*-4-BrPEAC		
Empirical formula	$C_8H_{11}BrClN$	$C_8H_{11}BrClN$	$C_8H_{11}BrClN$
Formula weight	236.54	236.54	236.54
Crystal system	monoclinic	monoclinic	monoclinic
Space group	$P2_1$	$P2_1$	$P2_1$
a/Å	5.4123(2)	5.47653(10)	5.5085(3)
b/Å	6.8976(2)	7.02250(13)	7.0764(4)
c/Å	13.0668(4)	13.0992(2)	13.1384(7)
α/deg	90	90	90
β/deg	93.236(8)	94.0673(16)	94.465(5)
γ/deg	90	90	90
Volume/Å^3	487.03(3)	502.511(15)	510.61(5)
Z	2	2	2
Goodness-of-fit on F^2	1.051	1.199	1.057
R_1	0.0449	0.0475	0.0517
wR_2	0.1279	0.1492	0.1585

Table S2. Crystal data and structure refinement of *S*-4-BrPEAC at 80 K, 300 K and 390 K.

Temperature/K	80	300	390
Compound	*S*-4-BrPEAC		
Empirical formula	$C_8H_{11}BrClN$	$C_8H_{11}BrClN$	$C_8H_{11}BrClN$
Formula weight	236.54	236.54	236.54
Crystal system	monoclinic	monoclinic	monoclinic
Space group	$P2_1$	$P2_1$	$P2_1$
a/Å	5.40890(10)	5.4758(2)	5.5054(4)
b/Å	6.8958(2)	7.0246(2)	7.0895(5)
c/Å	13.0697(3)	13.0918(4)	13.1417(10)
α/deg	90	90	90
β/deg	93.133(2)	94.062(3)	94.486(7)
γ/deg	90	90	90
Volume/Å^3	486.75(2)	502.32(3)	511.36(6)
Z	2	2	2
Goodness-of-fit on F^2	1.088	1.068	1.074
R_1	0.0554	0.0538	0.0692
wR_2	0.1608	0.1553	0.2008

Table S3. Crystal data and structure refinement of *Rac*-4-BrPEAC at 300 K.

Temperature/K	300
Compound	*Rac*-4-BrPEAC
Empirical formula	$C_8H_{11}BrClN$
Formula weight	236.54
Crystal system	orthorhombic
Space group	*Pccn*
a/Å	19.4511(12)
b/Å	14.2516(11)
c/Å	7.4067(6)
α/deg	90
β/deg	90
γ/deg	90
Volume/Å^3	2053.2(3)
Z	8
Goodness-of-fit on F^2	1.023
R_1	0.0508

wR_2	0.1537

Table S4. Comparison of the d_{33} value among different materials.

Compound	d_{33} (pC/N)	Ref.
(*R*-/*S*-α-PEA)$_2$TeI$_6$	2.6	6
RMBA-BF_3	3.5	7
4-AA	6	8
[(*S*)-NEA]$_4$[Bi_2Cl_{10}]	6.7	9
Rochelle salt	7	10
γ-glycine	10	11
R-/*S*- $MPCoCl_4$	10.5	12
[(*S*)-MPP][ClO_4]	18	13
TGS	20	14
R/*S*-MP-TFSA	20	15
D-ImCS	20	16
[(*R*)-3-hydroxy-pyrrolidinium]$_5$$Sb_4Br_{17}$	22	17
R-(4MeOPEA)$_2$$SnBr_6$	22.27	18
PVDF	28	19
(*R*-α-PEA)$_4$$Bi_2I_{10}$	32	20
(DMPA)$_3$$Bi_2Br_9$	35	21
(*R*-1,2-DAP·I)$_4$·I_3·BiI_6	35	22
(Cl-PA)$_2$$PbBr_4$	36	23
[(CF_3-C_6H_4-NH_3)(18-crown-6)][TFSA]	42	24
***R*/*S*-4-BrPEAC**	**49**	**This work**
NDABCO-NH_4-Br_3	63	25
(RM3HQ)$_2$$RbLa(NO_3)_6$	106	26
$HOCH_2(CF_2)_3CH_2OH$	138	27
TMCM-$CdCl_3$	383	14
TMCM-$CdCl_2Br$	440	28

References:

1. G. Kresse and J. Furthmuller, *Comp. Mater. Sci.*, 1996, **6**, 15-50.
2. G. Kresse and J. Furthmuller, *Phys. Rev. B*, 1996, **54**, 11169-11186.
3. J. P. Perdew, K. Burke and M. Ernzerhof, *Phys. Rev. Lett.*, 1996,**77**, 3865-3868.
4. Y. Le Page and P. Saxe, *Phys. Rev. B*, 2002, **65**, 104109.
5. X. Wu, D. Vanderbilt and D. R. Hamann, *Phys. Rev. B*, 2005,**72**, 035105.
6. K.-Z. Tao, Q. Li and Q.-F. Yan, *J. Phys. Chem. Lett.*, 2024, **15**, 6024-6030.
7. S. Sahoo, S. Mukherjee, V. B. Sharma, W. I. Hernández, A. C. Garcia-Castro, J. K. Zaręba, D. Kabra, G. Vaitheeswaran and R. Boomishankar, *Angew. Chem. Int. Ed.*, 2024, **63**, e202400366.
8. X.-J. Song, W.-B. Sun, L.-X. Zhou, W.-X. Mao, H.-M. Xu, J.-F. Lan, Y. Zhang and H.-Y. Zhang, *J. Am. Chem. Soc.*, 2024, **146**, 32519-32528.
9. S. K. Mahato.,V. Kushwaha.,J. K. Zaręba and R. Boomishankar, *Inorg. Chem.*, 2025, **64**,

21194-21203.

10. W.-Q. Liao, Y.-Y. Tang, P.-F. Li, Y.-M. You and R.-G. Xiong, *J. Am. Chem. Soc.*, 2018, **140**, 3975-3980.

11. R.-X. Wang, J.-J. Sui and X.-D. Wang, *ACS Nano*, 2022, **16**, 17708-17728.

12. B.-Y. Jian, X. Lv, L.-C. An and G.-M. Wang, *Small*, 2025, **21**, e08584.

13. S.-J. Yang, Y.-J. Bai, J.-C. Qi, X.-Y. Huang, X. Shen, Y-Z Lu, Z.-T. Xia, H.-P. Lv and W.-Q. Liao, *CrystEngComm*, 2024, **26**, 2883.

14. H.-P. Lv, W.-Q. Liao, Y.-M. You and R.-G. Xiong, *J. Am. Chem. Soc.*, 2022, **144**, 22325-22331.

15. S.-Z. Liu, W.-J. Ding, P.-F. Li, Z.-L. Liao, F.-X. Zhao, R.-Y. Bai, M.-D. Lu, H.-P. Lv, X.-G. Chen and Y. Ai, *ACS Appl. Mater. Interfaces*, 2025, **17**, 55153-55160.

16. L. Xu, X. Mu, X.-G. Chen, H.-Y. Zhang and R.-G. Xiong, *Chem. Mater.*, 2021, **33**, 5769-5779.

17. H.-Y. Shen, L. He, P.-P. Shi, Q. Ye, *J. Mater. Chem. C*, 2021, **9**, 4338-4343.

18. H.-R. Yang, X.-Q. Wei, G.-Z. Wang, C. Zhao, S.-S. Huang, Z.-G. Li and W. Li, *Chin. J. Chem.*, 2025, **43**, 3213-3220.

19. S. Mohammadpourfazeli, S. Arash, A. Ansari, S.-Y. Yang, K. Mallick, R. Bagherzadeh, *RSC Adv.*, 2023, **13**, 370–387.

20. K.-Z. Tao, B.-W. Zhang, Q. Li, Q.-F. Yan, *Small*, 2023, **19**, 2207663.

21. L. Pan, H.-F. Ni, P.-Z. Huang, H.-H. Li, M.-J. Lin, G. Teri, J.-Q. Luo, L.-K. Ye, J.-K. Xu, Q.-Q. Jia, C.-F. Wang, Z.-Q. Liu, Z.-X. Zhang, Y. Zhang, D.-W. Fu, *Angew. Chem. Int. Ed.*, 2025, DOI: 10.1002/anie.5334832.

22. C.-F. Wang, N. Wang, L. liu, L.-P. Miao, H.-Y. Ye, Y. Zhang, C. Shi, *Chin. Chem. Lett.*, 2023, **34**, 108051.

23. Y.-Y. He, S.-F. Wu, X.-F. Li, Q. Wang, R.-F. Zhao, L. Pan, C.-B. Qin, X.-M. Zhang and D.-Y. Fu, *Chem. Sci.*, 2025, **16**, 20948-20958.

24. H.-P. Lv, Y.-R. Li, X.-J. Song, N. Zhang, R.-G. Xiong, H.-Y. Zhang, *J. Am. Chem. Soc.*, 2023, **145**, 3187-3195.

25. H. Zhang, Z.-K. Xu, Z.-X. Wang, H. Yu, H.-P. Lv, P.-F. Li, W.-Q. Liao and R.-G. Xiong, *J. Am. Chem. Soc.*, 2023, **145**, 4892-4899.

26. C. Shi, J.-J. Ma, J.-Y. Jiang, M.-M. Hua, Q. Xu, H. Yu, Y. Zhang, H.-Y. Ye, *J. Am. Chem. Soc.*, 2020, **142**, 9634-9641.

27. H.-Y. Zhang, Y.-Y. Tang, Z.-X. Gu, P. Wang, X.-G. Chen, H.-P. Lv, P.-F. Li, Q. Jiang, N. Gu, S.-Q. Ren and R.-G. Xiong, *Science* 2024, **383**, 1492-1498.

28. X.-G. Chen, Y.-Y. Tang, H.-P. Lv, X.-J. Song, H. Peng, H. Yu, W.-Q. Liao, Y.-M. You and R.-G. Xiong, *J. Am. Chem. Soc.*, 2023, **145**, 1936-1944.